Calibrating the Swarm: Networked Small Satellite Magnetometers for Auroral Plasma Science

J. Brent Parham, Osi Van Dessel, Maria Kromis, Phillip Teng, Aleks Zosuls, Brian Walsh, Joshua Semeter
Boston University Center for Space Physics
8 Saint Mary's St., Boston, MA 02215; (857) 756-4693
jbparham@bu.edu

ABSTRACT

Motivated by small-scale auroral plasma science, ANDESITE, a 6U CubeSat with eight deployable picosatellites, will fly a network of magnetometers through the Northern Lights. With the spacecraft due to launch on the upcoming ELaNa XIX mission, this work details its science mission architecture along with the payload design and calibration. Each three-axis magnetometer instrument is hosted by a deployable picosatellite about the size of a piece of toast. Calibration of these sensors included a test of the integrated picosatelites in a Helmholz cage that sweeps a wide range of magnetic environments. Here, we show that even in the small package—operating under a watt with a compact power system, radio, gyro, and GPS—we were able to sample at greater than 30 Hz with an uncertainty under 20 nT. We also present analysis for the entire network to understand the spatial frequency response of the kilometer-scale 3D filter created by the swarm as it flies through various current density structures in the ionospheric plasma.

INTRODUCTION

Spacecraft have been essential to understanding the auroral current system since the early days of spaceflight. The modern understanding mostly comes from such space-based sensors and offers a big picture of a closed current loop that connects the magnetosphere to the ionosphere. While the main structure was postulated early in the 20th century[1], strong evidence supporting the theory arrived with the coming of the space race.

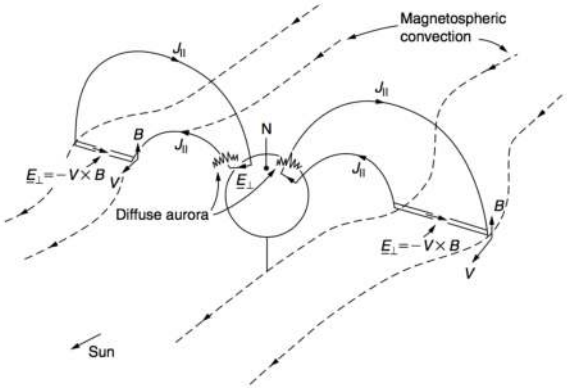

Figure 1: Schematic of auroral zone flux tubes, note the connection to the outer magnetosphere[2]

The system consists of a few main currents: $\mathbf{J}_\parallel$ flows that move parallel to the Earths dipolar magnetic field (Figure 1), and a closure set of currents in the ionosphere through resistive loading governed by the Pederson conductance. To better understand why the space race influenced our understanding of these currents, we need to understand what we can measure. If we assume that current is not generated in the closed volume around the auroral region, we can divide the current flows into the portion that is parallel to $\mathbf{B}$ and perpendicular and equalize them as follows

$$\nabla \cdot \mathbf{J} = \nabla_\perp \cdot \mathbf{J}_\perp + \frac{\partial J_\parallel}{\partial s} = 0 \tag{1}$$

where s is the field aligned coordinate. Assuming that the current perpendicular is only from the closure over the ionospheric height, Δs, we can integrate Eq. 1—with the Pederson current dominating and $E_\perp$ a dawn to dusk electric field

$$\begin{aligned} J_\parallel &= \int_{\Delta s} \nabla_\perp \cdot \mathbf{J}_\perp \mathrm{d}s \\ &= \int_{\Delta s} \nabla_\perp \cdot (\sigma_p \mathbf{E}_\perp) \mathrm{d}s \\ &= \nabla_\perp \cdot (\Sigma_p \mathbf{E}_\perp) \end{aligned} \tag{2}$$

Now we can use this form to inspect what we could actually measure in the system.

The right-hand side components of Eq. 2, $\sigma_p \mathbf{E}_\perp$, can be estimated with ground-based techniques such as Total Electron Content (TEC) measurements, magnetometer networks and Incoherent Scatter Radar (ISR) probes[3], but the left-hand side requires a space-based sensor since the current systems do not reach the ground. That measurement usually is taken by sampling the field with a magnetometer. Through Ampere's law we can map deflections about the Earth's dipole field $\mathbf{B}_0$ to currents and then any perturbations $\delta\mathbf{B}$ perpendicular to that dipole could be caused by parallel currents as in Eq. 3.

$$\begin{aligned} \nabla \times (\mathbf{B}_0 + \delta\mathbf{B}) &= \mu_0 \mathbf{J} \\ \nabla \times (\delta\mathbf{B}_\perp) &= \mu_0 \mathbf{J}_\parallel \end{aligned} \tag{3}$$

Over the years, magnetometer sensitivity and temporal resolution have improved, but decoupling spatial-temporal ambiguities in the measurements has been prohibited due to the high cost of spacecraft networks. In the next section, we review past missions for auroral measurements of the nature described above. After that review, we then analyze Boston University's small satellite mission ANDESITE to better understand its ability to overcome this instrumentation hurdle.

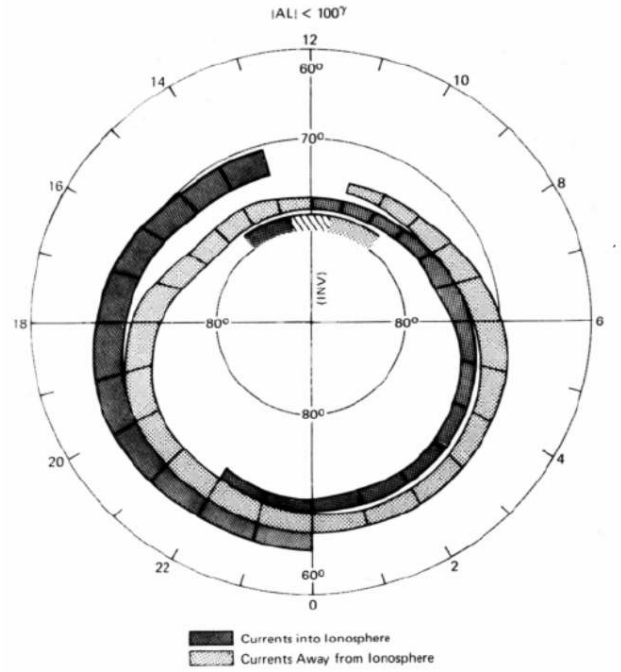

Figure 2: Summary of TRIAD data for field-aligned currents, plotted in magnetic latitude and local time where up is noon[4].

PREVIOUS SPACE-BASED MEASUREMENTS

Early in the space age, satellites have hosted plasma sensors for the purpose of teasing out quantities, like this field-aligned current. One of the first was the TRIAD mission in the 1970s, which hosted a magnetometer[4]. These data from TRIAD were a detailed time samplings, without good absolute calibration, but with processing they could show gross auroral topology by using many orbits of data with assumptions restricting the single point perpendicular magnetic field measurements along the satellite trajectory to the local parallel currents (Figure 2). Often this mapping was made by assuming a steady in-time-and-space system that behaved like an infinite sheet of current density. With those assumptions, the spatial-temporal ambiguity due to satellite trajectory and discrete sampling in time is ignored, and you can recover an estimate of currents by

$$\frac{\partial}{\partial x}\delta B_y = \mu_0 J_z \tag{4}$$

where the x-coordinate is aligned with the satellites trajectory, z is along $\mathbf{B}_0$, and y completes the right-handed system. With the satellite velocity $\frac{\mathrm{d}x}{\mathrm{d}t} = v_s$ you can rewrite a manipulation of time series data as

$$\frac{1}{v_s}\frac{d}{dt}\delta B_y(t) = \mu_0 J_z \tag{5}$$

This represents about the best that can be done when attempting to map between quantities using single sensor measurements. It inherently includes an ambiguity as to whether a measured deflection is a temporal variation or spatial. As measurements were collected with single sensors such as this[5,6] the signal processing techniques evolved, increasing the sensitivity and resolution of the time series, but were ultimately limited by these assumptions. It became clear that spacecraft were measuring phenomena on scales where this spatial smearing was affecting the results.

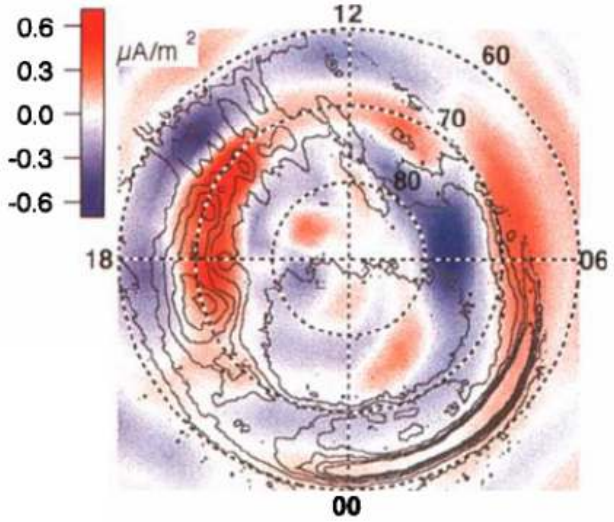

Figure 3: Current density estimate from early in the AMPERE project shown in the same coordinates as the TRIAD data. Red coloring indicates currents away from the ionosphere[7].

Several missions were designed with multiple spacecraft on slightly different orbits to tease out the space-time ambiguity. One of the early missions of this nature used engineering magnetometers already on the Iridium satellite constellation in what is known as the AMPERE project[7]. Data collected from 66+ satellites over six polar orbital planes is mapped to a vector potential estimate of the global magnetic disturbance. This disturbance is then used directly with Ampere's law to calculate a coarse map of the dynamic global current system,

as seen in Figure 3. The underlying mathematics relied on representing field-aligned currents to a poloidal vector potential that represented the deflections of the magnetic field. That representation simplified to a direct relation between a fit of magnetometer data $\delta\mathbf{B}_k$ at each satellite point k, Eq. 6, to a global scalar potential $\Psi(r,\theta,\phi)$ represented by spherical harmonics and a Poisson equation for current density, Eq. 7.

$$\min_{\Psi} |\delta\mathbf{B}_k - \mu_0 \hat{r} \times \nabla\Psi|_k^2, \quad \forall k \tag{6}$$

$$\mathbf{J} = \nabla \cdot \nabla\Psi = \nabla^2\Psi \tag{7}$$

While these data were reasonable for a global view, it did not have the resolution to show the small-scale phenomena that was postulated from early measurements. Around the same time as the beginning of the AMPERE project, Stasiewicz summarized evidence that high-frequency disturbances that were seen in scientific magnetometers were related to local Alfvén waves[8]. An early test of this involved comparing the ratio of the magnetic field to the electric field perturbations. Taking Eq. 3, and assuming that the perpendicular $\mathbf{E}_\perp$ and a Pederson conductivity are directly balanced by the current related to the measured deflections by the satellites in the sheet we see the following.

$$B_\perp = J_\perp = \mu_0 \Sigma_p E_\perp$$

$$\frac{E_\perp}{B_\perp} = \frac{1}{\mu_0 \Sigma_p} \propto v_A \tag{8}$$

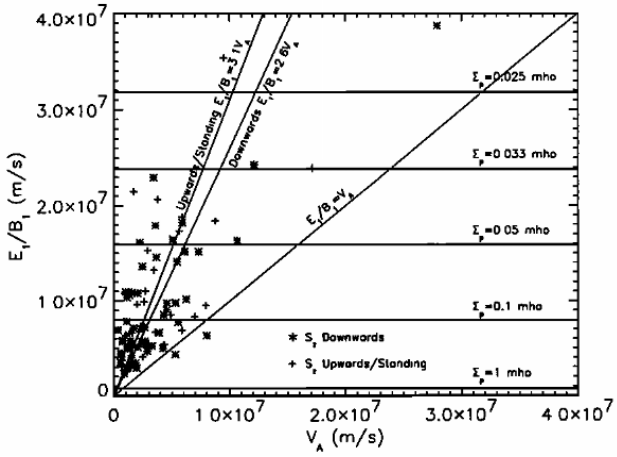

Figure 4: FAST measured $\frac{E_\perp}{B_\perp}$ compared to a local Alfvén speed calculated from particle measurements[5].

If the perturbations are related to the Alfvén wavemode, then this ratio should be correlated with the Alfvén speed, $v_A = B/\sqrt{\mu_0\rho}$ where ρ is the mass density. NASA's FAST spacecraft flew in a polar low earth orbit and saw many cases where this correlation was observed (Figure 4). But without a way to conduct the same spatial analysis as AMPERE on small scales, it remained difficult to accumulate more evidence.

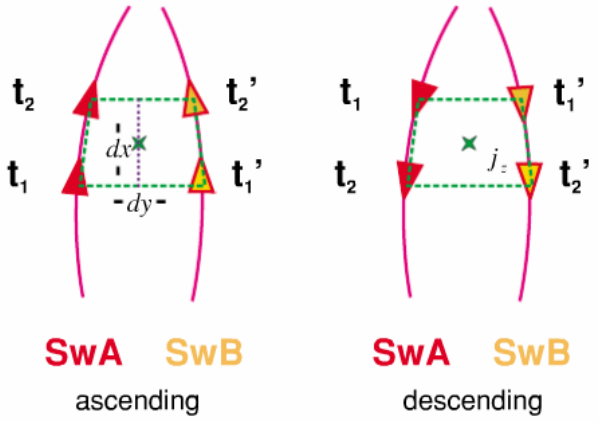

Figure 5: Local SWARM orbital configuration. SwA and SwB fly next to each other, and by using measurements from two time points a loop is created that can be used to estimate current density through the enclosed area[9]

Since those first analyses, several missions were developed including ESA's SWARM (two spacecraft)[9] and NASA's ST5[10] (three spacecraft) flying in tight formation, as an attempt to resolve first-order spatial variations as they flew through the aurora. The three ST5 satellites fly in the same orbit, one after the other, to correct for variability lost with a single satellite. A snapshot in time across the same orbital track allows for analysis of the spatial variability decoupled from the satellites velocity, removing that ambiguity introduced in Eq. 5. The SWARM mission, however, flies two spacecraft side by side to capture a spatial variability perpendicular to the orbital velocity. Their mission directly estimates the currents by assuming a relatively (when compared to the time scale of the orbital velocity) time-steady aurora, and creating a geometrical loop that can be used to evaluate a discrete approximation to the integral form of Amperes law, as seen in Eq. 9 and Figure 5.

$$\int\int \mathbf{J} \cdot d\mathbf{A} = \frac{1}{\mu_0} \oint \mathbf{B} \cdot d\mathbf{l} \tag{9}$$

Boston University's ANDESITE mission aims to connect these two methodologies to allow for better space-time decoupling. By using several small sensor nodes deployed from a main bus, higher data-sampling density can be achieved while allowing for fewer assumptions on the geometry of the current sheet present. In the next

sections we will cover a description of the methodology and projected capability of the system.

METHODOLOGY

ANDESITE

ANDESITE leverages many capabilities that have come about from commercial and academic interest in small satellite technology while ultimately remaining a very simple scientific approach—networked magnetometers. It is designed within the CubeSat standard, fitting in the "6U" form factor (20 cm $\times$ 30 cm $\times$ 10 cm) for a Planetary Systems Corporation Canisterized Satellite Dispenser (CSD), relying on many commercially available subsystems for it's operation, and therefore has proven to be inexpensive when compared to larger multipoint sampling missions. The mission is currently slated for launch in 2017 through NASA's Educational Launch of Nano-satellites (ELaNa) program.

(a) 6U CubeSat Mule **(b) Sensor Node**

Figure 6: Engineering models of satellite system

Figure 7: ANDESITE deployment configuration (separation distances not to scale)

Once deployed from the launch vehicle, every few orbits the main 6U spacecraft bus or "Mule" (Figure 6a) deploys pairs of smaller Sensor Nodes (Figure 6b). These nodes each contain a three-axis magnetometer and relay their measurements back to the Mule which communicates the data to ground through the GlobalStar communication network via a NearSpace Launch EyeStar Duplex radio.

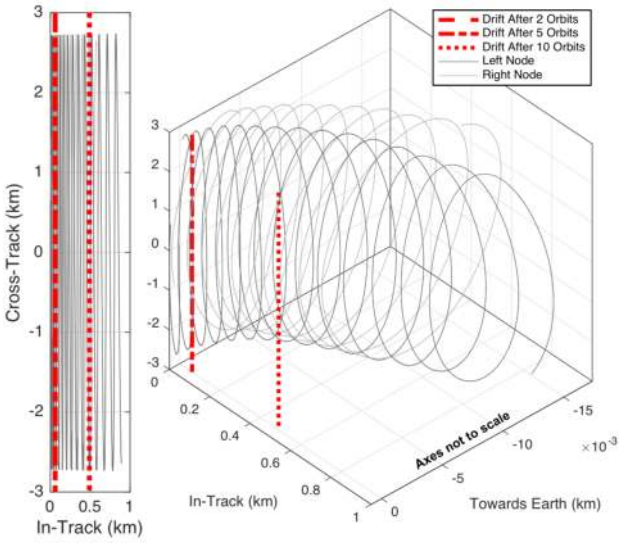

Figure 8: A numerical model of single Node-pair deployment shows the drift of the Nodes as they are referenced to the Mule's body-fixed coordinates. The red dashed lines show the total drift after a few orbits and the right plot helps visualize the trajectory by changing the scale of the cross-track axes.

Due to differential drag between the Mule and Nodes slowly drift apart and create a spatial grid that samples in- and cross-orbital track. This is shown in Figure 7 which was created using the NRLMSISE-00 atmosphere and a 70 x 70 degree/order gravity model to propagate the spacecraft. The resulting formation effectively combines the geometric concepts of SWARM and ST5.

In-track separation can be controlled by time of the Node releases, which is adjustable on-orbit, and a designed cross-track separation of 5 km is set by the spring constant of the ejection mechanism (seen in Figure 8), but for this analysis we will vary it to understand the limitations of the design choice. Our ultimate goal is to parameterize the sensor network's geometry and attempt to understand the limits of it's resolution, thereby assessing it's relevance to scientific measurement.

Science Instrument

I Design

Since the mission payload is to take magnetic field measurements, certain design considerations were included in the final sensor node design to ensure the cleanest signal in compact size constraint. The magnetometers chosen on board the sensor node boards are the HMC1001 and HMC1002, 1-axis and 2-axis magnetic sensors, respectively. They provide the full-scale range of $\pm$ 2 gauss

(± 200,000 nT) and have a resolution of 85 μgauss (8.5 nT). The supporting circuitry includes a deguassing circuit that sends a 5V set and reset circuit through the magnetometers for 2 microseconds.The offset straps are ignored and corrections will be done after the data is transferred back.

The differential outputs of the magnetometers are connected to an analog low-pass filter and the resistors are metal film to minimize noise. The differential outputs are fed into an ADS1248, a 24-bit delta-sigma analog-to-Digital converter with a programmable gain amplifier. The programmable amplifier was set to 64 times to account for the full-scale range of the magnetometers. For the voltage reference into the ADC, the ADR441 was selected for its low-noise and low-temperature coefficient of 3 ppm/°C.

Since the sensor node board includes many noisy digital components, a separate power supply was dedicated to the magnetometers, analog to digital converter, and voltage reference. The LM2731 boost converter brings the battery voltage up to 8.5 V and then the ADP3333 provides the 5.0 V power line for the science instrument.

To minimize the effect of ground loops, all ground planes are removed in the area around the magnetometers. All the power supply integrated circuits (IC) are placed as far away from the magnetic sensors and shielded with RF shields. Due to the constraint of space, the magnetometers are still in close proximity with shielded inductors from the solar panels. Ground-based calibration will include characterization of the temperature drift and any induced currents through the solar panels caused by the nodes rotation.

To ensure the orthogonality of the sensors after intense vibrational forces, ceramic blocks were machined and epoxied to the sensors.

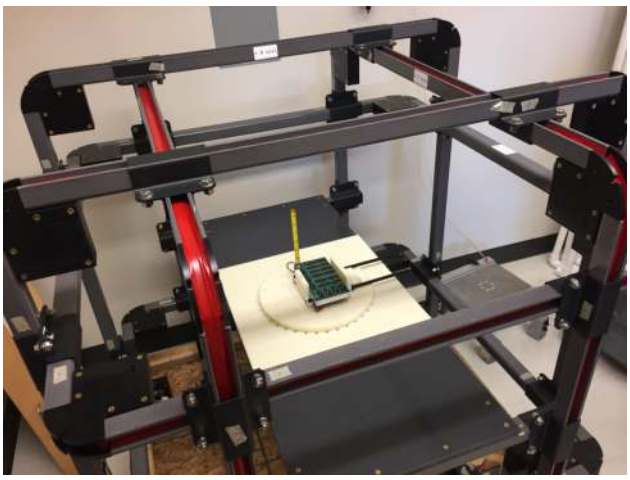

Figure 9: Sensor Node in the calibration Helmholtz cage test setup

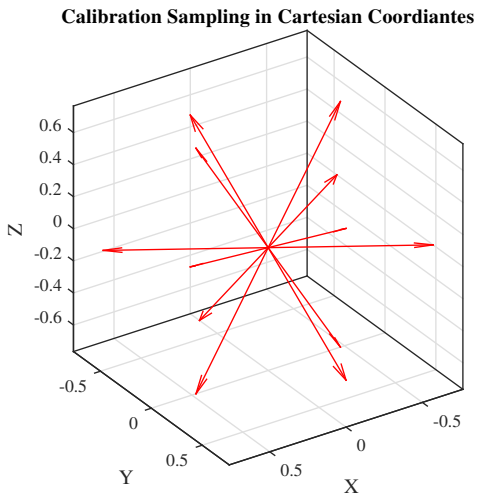

Figure 10: Commanded directions for magnetic field during calibration of magnetometer misalignment

II Calibration

Proper understanding of our on-orbit measurements is only achieved by thorough calibration of each node as it is built. From previous work with magnetometers we realized the importance of understanding the misalignment of three sampled axes and the performance of the sensors over the entire dynamic range expected. This section details our efforts to take enough data on each node to ensure we can properly understand our capabilities before ANDESITE is shipped.

To characterize the payload magnetometers we use a precision controlled 1.2 meter Helmholtz cage developed by Billingsley Aerospace and Defense as seen in Figure 9. Within the cage a non-magnetic test stand keeps the Sensor Node in alignment as various external fields are commanded. To coarsely characterize each axis, we command the coils along the three body axes of the spacecraft sweeping from -60,000 nT to + 60,000 nT in evenly space incremental steps. Holding each step for three seconds while sampling at a rate of 30 Hz we collect data continuously. Between each step we zero the cage and let it settle for three seconds and check for hysteresis of the measurements.

The standard deviation of each sampled step gives a useful metric to perform a weighted least squares fit of a calibration curve for the measurements mapped to the spacecraft body frame—positive x-axis along the long axis of the Sensor Node and positive z-axis towards the floor in Figure 9. The results of these fits and the associated uncertainties calculated for each axis at each commanded external field are shown in Figure 11. Note each axis is able to sample with a precision less than 10 nT.

To store more data for an effort at determining the corrections for non-orthogonality, the calibration script

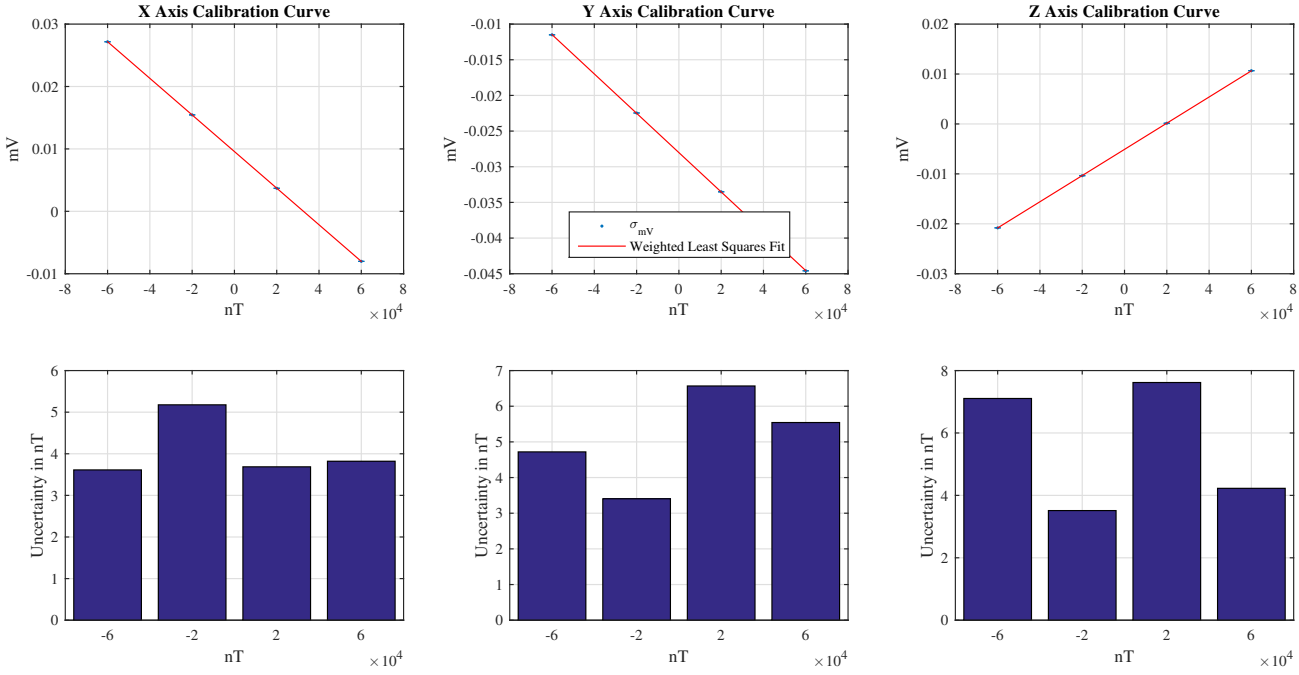

Figure 11: Magnetometer calibration for each principle coordinate of the Sensor Node body axes (top plots) and associated instrument uncertainty converted from the analog-to-digital-converter outputs in mV to nT as a function of commanded test field strength (bottom plot). For all figures, the x-axis is the Helmholz cage's commanded field strength.

then commands the coil to sweep through various measurement angles that sample uniformly about a geodesic sphere with 12 points, seen in Figure 10. The magnitudes of each vector use the same sweep as the coarse calibration resulting in 48 data points for each axis in spherical coordinates r, ϕ and θ, where r is the axis measurement magnitude and the unit vector is determined by the coarse calibration curves. Each axis can be fit to a spherical harmonic expansion of degree and order 4, against the commanded vector from the Helmholtz cage. This allows a mapping from the measured mis-aligned raw measurements to a corrected vector measurement.

Mathematical Framework for Current Estimates

Let's start with a very simple model for field aligned currents on a dipole directly from Ampere's law in a magnetically aligned spherical coordinate system

$$\begin{aligned}\nabla \times (\delta \mathbf{B}) &= \mu_0 \mathbf{J}_{\parallel} = \mu_0 J_{\parallel} \hat{\mathbf{B}}_0 \\ &= \mu_0 J_{\parallel}(r,\theta,\phi)\frac{(2\cos\phi)\hat{\mathbf{r}} + (\sin\phi)\hat{\phi}}{\sqrt{3\cos^2\phi + 1}}\end{aligned}$$

The relevant parts of the curl operator in spherical coordinates become (for simplicity $\delta\mathbf{B} = [B_r, B_\theta, B_\phi]$)

$$\begin{aligned}\nabla \times (\delta \mathbf{B}) =& \frac{1}{r\sin\phi}\left[\frac{\partial}{\partial\phi}(\sin\phi B_\theta) - \frac{\partial B_\phi}{\partial\theta}\right]\hat{\mathbf{r}} + \\ & \frac{1}{r}\left[\frac{1}{\sin\phi}\frac{\partial B_r}{\partial\theta} - \frac{\partial}{\partial r}(rB_\theta)\right]\hat{\phi}\end{aligned}$$

and rewriting in matrix form

$$\begin{aligned}&\begin{bmatrix} \frac{1}{r\sin\phi}\left(\frac{\partial}{\partial\phi}(\sin\phi B_\theta) - \frac{\partial B_\phi}{\partial\theta}\right) \\ \frac{1}{r}\left(\frac{1}{\sin\phi}\frac{\partial B_r}{\partial\theta} - \frac{\partial}{\partial r}(rB_\theta)\right)\end{bmatrix} = \\ &\qquad \frac{\mu_0 J_{\parallel}(r,\theta,\phi)}{\sqrt{3\cos^2\phi+1}}\begin{bmatrix}2\cos\phi \\ \sin\phi\end{bmatrix}\end{aligned} \tag{10}$$

We can then try to simplify and solve each component individually, the components follow as

$$\begin{aligned}\frac{\partial}{\partial\phi}(\sin\phi B_\theta) - \frac{\partial B_\phi}{\partial\theta} &= \mu_0 J_{\parallel}(r,\theta,\phi)\frac{r\sin(2\phi)}{\sqrt{3\cos^2\phi+1}} \\ \frac{1}{\sin\phi}\frac{\partial B_r}{\partial\theta} - \frac{\partial}{\partial r}(rB_\theta) &= \mu_0 J_{\parallel}(r,\theta,\phi)\frac{r\sin\phi}{\sqrt{3\cos^2\phi+1}}\end{aligned}$$

Assuming only variations of any parameter in the latitude angle (ϕ)

$$\frac{\partial}{\partial\phi}(\sin\phi B_\theta) = \mu_0 J_\parallel(\phi)\frac{r\sin(2\phi)}{\sqrt{3\cos^2\phi+1}}$$

$$B_\theta = \frac{\mu_0}{\sin\phi}\int\left(J_\parallel(\phi)\frac{r\sin(2\phi)}{\sqrt{3\cos^2\phi+1}}\right)\mathrm{d}\phi$$

Initial inspection shows that we should only expect a magnetic deflection in the longitudinal angle (θ) as the spacecraft flies through a current sheet that only varies through latitude. For sanity sake, check this equation near the pole to see a geometry where the magnetic direction is directly down—using a small angle approximation $\phi \to 0$ and constant current.

$$B_\theta = \frac{\mu_0}{\phi}\int J_\parallel r\phi \mathrm{d}\phi = \mu_0 J_\parallel \frac{r\phi}{2} \tag{11}$$

This is analogous to the solution for an infinite current sheet in Cartesian coordinates, where $r\phi$ is the distance in the direction perpendicular to the sheet. The variation of the magnetic measurement mostly occurs in the latitudinal direction, which informs a design choice to have more sampling in that direction. ANDESITE therefore was designed with that in mind and the following section will lay out a framework for spacing the measurements to best capture the variation.

For an arbitrary satellite-based sensor arrangement, like ANDESITE, it is difficult to work with Ampere's law in the differential form consistently—similar to difficulties unstructured grids in computational physics. To help with that lack of order, we return to the integral form in Eq. 9. From here on we will drop the δ and assume all measurements are the perturbations due to currents. To make a closed loop, all that is needed is a set of three axis magnetometer measurements $\mathbf{B}_i$ and the positions of the satellites. With that, a triangle can be constructed as in Figure 12, where $\mathbf{r}_{ij} = \mathbf{r}_j - \mathbf{r}_i$ is the vector difference between satellite positions.

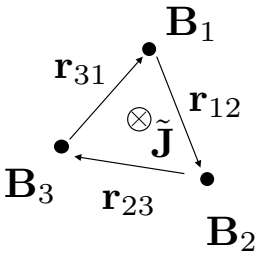

Figure 12: Arrangement for simplest application discrete Ampere's law

We can then write a discrete form of the integrals in Eq. 9 in a way analogous to a finite volume numerical scheme representation.

$$\left(\frac{\mathbf{B_1}+\mathbf{B_2}}{2}\right)\cdot\mathbf{r}_{12} + \left(\frac{\mathbf{B_2}+\mathbf{B_3}}{2}\right)\cdot\mathbf{r}_{23} + \left(\frac{\mathbf{B_3}+\mathbf{B_1}}{2}\right)\cdot\mathbf{r}_{31} = -\mu_0\tilde{J}\frac{|\mathbf{r}_1 2\times\mathbf{r}_1 3|}{2} \tag{12}$$

If we have an arbitrary collection of satellites, we can then form a collection of triangles using a Delaunay mesh. From that mesh then calculate a set of currents passing through the centroid of each triangle.

To interpolate, fit a Fourier series representation of current density to the mesh. As an example, the following assumes a 2D sampling, which is a good assumption for a small spacecraft formation flying at the same altitude.

In this scenario all currents estimated are radial and we can fit for just a scalar representation in two local dimensions x and y that are perpendicular to the radial vector—where $j = \sqrt{-1}$, and $k_{m,n}$ are wavenumbers dictated by the measurement capability of the sampling geometry.

$$J_{\text{model}} = \langle J\rangle + \sum_{m,n} c_{mn} e^{(jk_m x + jk_n y)} \tag{13}$$

$$\langle J\rangle = \frac{1}{N}\sum_{i=1}^{N}\tilde{J}_i$$

Finally minimize the error between a model of the current field and the measurements $\tilde{J}_i$ from Eq. 12, where each location is defined as the centroid of the i-th triangle that was used to calculate it: $[x_i, y_i]^T = (\mathbf{r}_{1,i} + \mathbf{r}_{2,i} + \mathbf{r}_{3,i})/3$. A cost function could be of the form below, with additional physical constraints (such as a divergence free current constraint shown notionally below if we can construct a modeled vector field, $\mathbf{J}$).

$$\min_{c_{nm}}\left(|\tilde{J}_i - J_{\text{model}}(x_i,y_i)|^2 + \alpha|\nabla\cdot\mathbf{J}(x_i,y_i)|^2\right) \tag{14}$$

For the rest of this paper we will just estimate the convergence of $\tilde{J}_i$ into the true field as we change the geometry for a parameterized ANDESITE swarm configuration.

RESULTS

To test the recovery of current density, we first set up a simple model for spatial variations of current. Assuming multiple wave-numbers in each direction we can use

$$J(x,y) = J_0\sum_{m,n} s_{mn} e^{(jk_m x + jk_n y)} \tag{15}$$

where J_0 is a maximum current amplitude, here chosen to be 0.2 μA/m^2 and the coefficients are $s_{mn} = 1$ representing a white noise power spectrum where all frequencies have equal contribution to field. To solve for deflections, we need to map to a scalar potential as follows

$$\nabla^2 \Psi = J \tag{16}$$

$$\mathbf{B} = \mu_0 \hat{r} \times \nabla \Psi \tag{17}$$

Resulting in an analytical expression for $\mathbf{B}(x, y)$ based on our definition of current, $J(x, y)$. As a Fourier series it is expressed as Eq. 18.

$$\mathbf{B} = \mu_0 J_0 \sum_{m,n} \begin{bmatrix} jk_n \\ -jk_m \end{bmatrix} \frac{s_{mn}}{k_m^2 + k_n^2} e^{(jk_m x + jk_n y)} \tag{18}$$

This deflection map, that satisfies Amperes law, is fed through the scheme. Through use of an analytical truth, we can gauge the effectiveness of the satellite swarm sampling method directly before flight. An example of a postulated swarm geometry on top of this analytical set of fields is shown in Figure 13. The nodes of the swarm form triangles and the current estimates are assumed to be at the center of the triangles points T1-T7. To estimate error we use a normalized difference between the actual field and the estimated field. Then a single number for the error of the estimate is calculated by averaging across all the points, represented by Eq. 19.

$$\left\langle \left| \frac{\tilde{J}_i - J(x_i, y_i)}{J(x_i, y_i)} \right| \right\rangle = \frac{1}{7} \sum_{i=1}^{7} \left| \frac{\tilde{J}_i - J(x_i, y_i)}{J(x_i, y_i)} \right| \tag{19}$$

Numerical Parameterization

We can think of the satellite swarm as a 2D linear spatial filter of the current. With that in mind, it is apparent to approach performance in therms of a frequency response. By sweeping across spatial frequencies, each axis independently, we can fully characterize the performance. Figure 14, shows an example sweep in terms of a spatial wavelength for the nominal formation shown in Figure 13.

Note that ANDESITE should have better performance in the y-direction, which intuitively makes sense because of the higher spatial sampling density. We can also gain insight from thinking the of the system as a high-pass filter, where we can sample anything that has frequencies above the characteristic lengths of the satellite spacings. In turn, those spacings determine the bands that we can reliably reconstruct from the measurements.

Key to this analysis is our reliance on a normalized error. All the plots represent performance loss that occurs solely due to an effective discretization error and is agnostic of sensor sensitivity or field magnitudes. We can therefore apply the generalized method to any spatial sampling method regardless of strength or shape of the perturbations. To inform a magnetometer design we would need to know absolute shape, size and current density of structures we would want to find.

Taking the numerical experiment a step further, we can tweak the in-track separation which can be deter-

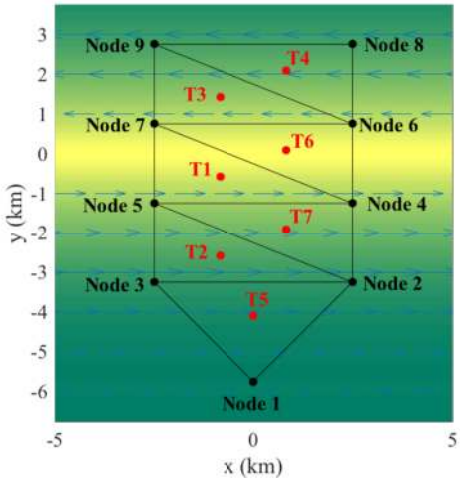

Figure 13: ANDESITE formation and Delaunay triangulation created by satellite nodes, the arrows represent the magnetic deflection due to radial currents represented by the color map. Positive currents are toward the reader.

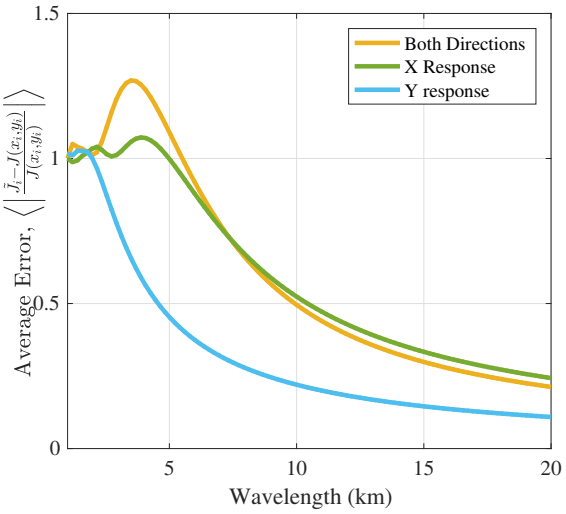

Figure 14: Frequency response for the spatial filter defined by the swarm gemoetry of Figure 13. Note the y-axis performs better than the x-axis in recovering the current.

mined by our sensor node deployment times—a parameter that can be changed on orbit. Over this design space—characteristic wavelengths and separation distance—Figure 15 shows contours of constant error. This plot can be used to explore the design space. For instance if a error is desired to be below 20% for 10 km waves, then the node in-track separation should be about 2 km.

Physical Relevance

Figure 16 shows a time and length scales for various dynamic processes that propagate along field lines in the local plasma. These curves come from the dispersion relations derived using the atmospheric conditions on a typical night side at 70° latitude and 500 km altitude. ANDESITE can collect data at a rate of 30 Hz—the region of the graph not grayed out. This region in the 10-100 km length scale includes local Alfvén waves which encompasses the design space of the formation spacing explored in the previous section.

CONCLUSION

Within this paper we explored the previous work towards understanding the auroral current systems. Following the progression to ever high resolutions from the initial data from TRIAD to AMPERE and FAST we can see that as the data becomes more detailed we are driven to need measurements at smaller scales. ANDESITE was designed to push the limits of spatial resolution and here we developed a rigorous methodology to examine the performance of satellite swarms like it. In doing so we proved the capability of the system to resolve kilometer scale phenomena that include the domain of in situ Alfvén waves. Future work along this direction will be to better understand the role of measurement uncertainty in the metric defined herein. Through understanding the uncertainty we can then better inform the magnetometer design for future mission and rigorously examine the one chosen for ANDESITE.

References

[1] Birkeland, K., *The Norwegian Aurora Polaris Expedition 1902-1903: On the Cause of Magnetic Storms and the Origin of Terrestrial Magnetism*, 1908.

[2] Kelley, M. C., *The Earth's Ionosphere: Plasma Physics & Electrodynamics*, Vol. 96, 2009.

[3] Nicolls, M. J., Cosgrove, R., and Bahcivan, H., "Estimating the Vector Electric Field Using Monostatic, Multibeam Incoherent Scatter Radar Measurements," *Radio Sci*, Vol. 49, No. 11, 2014, pp. 1124–1139. doi:10.1002/2014rs005519.

[4] Iijima, T. and Potemra, T., "Field-Aligned Currents in the Dayside Cusp Observed by Triad," Vol. 81, No. 34, 1976, pp. 5971–5979. doi:10.1029/JA081i034p05971.

[5] Chaston, C. C., Carlson, C. W., Peria, W. J., Ergun, R. E., and P., M. J., "FAST Observations of Inertial Alfven Waves in the Dayside Aurora," *Geophys Res Lett*, Vol. 26, No. 6, 1999, pp. 647–650. doi:10.1029/1998gl900246.

[6] Team, F., "Magnetic Field Experiment on the Freja Satellite," Vol. 70, No. 3-4, 1994, pp. 465–482. doi:10.1007/BF00756882.

[7] Waters, C., Anderson, B., and Liou, K., "Estimation of Global Field Aligned Currents Using the Iridium® System Magnetometer Data," *Geophys Res Lett*, Vol. 28, No. 11, 2001, pp. 2165–2168. doi:10.1029/2000gl012725.

[8] Stasiewicz, K., Bellan, P., Chaston, C., and Kletzing, C., "Small Scale Alfvénic Structure in the Aurora," *Space Science*, 2000.

[9] Ritter, P. and Lühr, H., "Curl-B Technique Applied to Swarm Constellation for Determining Field-Aligned Currents," *Earth*, Vol. 58, No. 4, 2006, pp. 463–476. doi:10.1186/BF03351942.

[10] Cumnock, J., Le, G., Imber, S., Slavin, J., Zhang, Y., and Paxton, L., "Space Technology 5 Multipoint Observations of Transpolar Arc–Related FieldAligned Currents," Vol. 116, No. A2, 2011. doi:10.1029/2010JA015912.

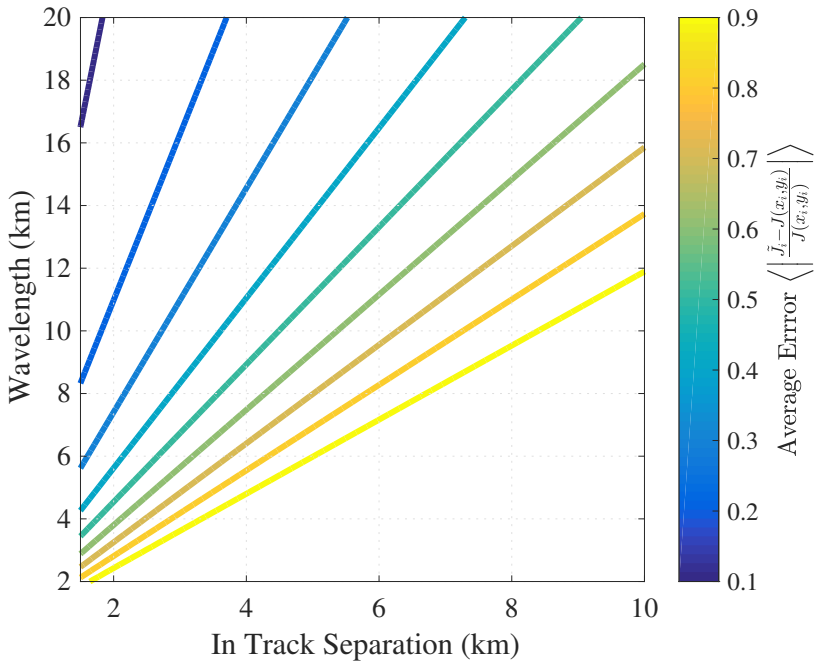

Figure 15: Contours of constant error while varying the frequency of perturbations and the in-track separation (y-axis spacing) of the formation.

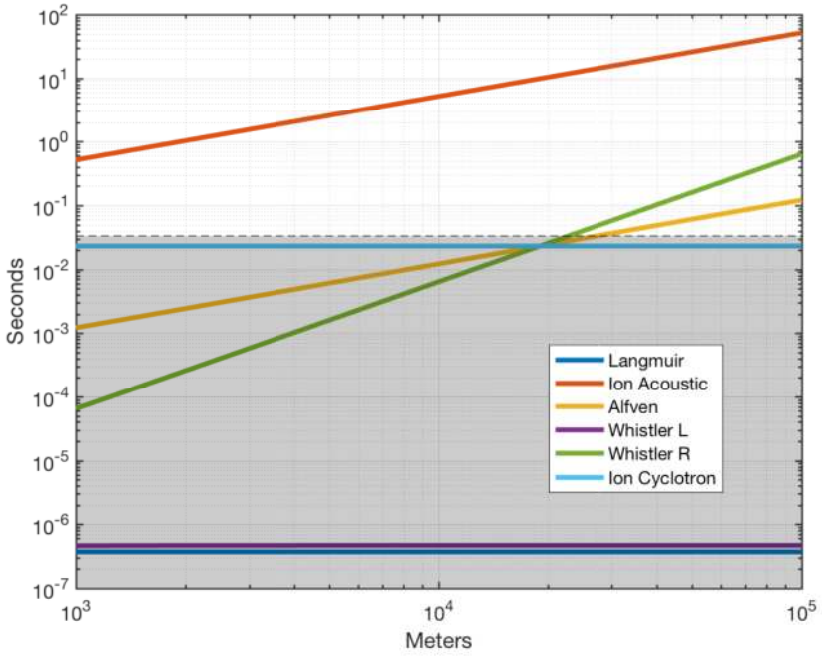

Figure 16: Time and length scales for various dynamic wave phenomena that propagate along the field lines. They grayed area is faster than the data rate of ANDESITE.